Check for updates

International Journal of Energy Research

WILEY

RESEARCH ARTICLE OPEN ACCESS

Tailored Electrodeposition for Scalable Fabrication of Uniform and High-Efficiency Large-Area Electrodes for PEM Water Electrolysis

Joon-Young Park | Kyeong-Rim Yeo | Soo-Kil Kim

School of Integrative Engineering, Chung-Ang University, 84 Heukseok-ro, Dongjak-gu, Seoul 06974, Republic of Korea

Correspondence: Soo-Kil Kim (sookilkim@cau.ac.kr)

Received: 2 October 2025 | **Revised:** 4 January 2026 | **Accepted:** 12 February 2026

Academic Editor: Arnab Biswas

Keywords: Cu–Ni–Mo alloy catalyst | electrodeposition | hydrogen evolution reaction | process parameter | proton exchange membrane water electrolysis | scale-up

ABSTRACT

Water electrolysis is a promising route for large-scale hydrogen production, offering high-purity output, CO_2-free emissions, and compatibility with renewable energy integration. Among various fabrication techniques, electrodeposition provides a cost-effective, tunable, and binder-free method for producing high-performance electrodes. However, achieving consistent catalyst properties across large electrode areas remains a major challenge in scaling up electrochemical devices such as proton exchange membrane water electrolyzers (PEMWEs). This study presents a systematic electrodeposition approach for fabricating large-area Cu–Ni–Mo alloy catalysts with homogeneous composition and electrochemical performance across the electrode surface, guided by a previously optimized small-area reference. A custom-designed deposition cell enabled independent control of deposition parameters, and the effects of each parameter on catalyst composition, morphology, and hydrogen evolution reaction (HER) activity were thoroughly evaluated. As the electrode area increased, structural modifications to the deposition cell and electrode configurations required adjusting the deposition potential to maintain equivalent deposition conditions. The working–reference electrode distance was identified as a critical parameter that significantly influenced the actual deposition potential and resulting catalyst properties, while the working–counter electrode distance affected deposition uniformity through changes in ion transport dynamics. Under optimized conditions, a 10.2 cm^2 electrode was fabricated and evaluated through subdivided PEMWE tests, yielding consistent performance (2.00 to 2.03 V_{cell} at 2 A cm^{-2}) with only minor deviation from the reference catalyst. Scaling up further to 50 cm^2 yielded an average HER overpotential of 18.3 mV at −10 mA cm^{-2} and maintained excellent uniformity across the electrode. These findings offer a practical and adaptable methodology for fabricating large-area alloy electrodes with reproducible performance, advancing the scalable deployment of multicomponent catalysts for PEMWE.

1 | Introduction

To address critical sustainability challenges such as environmental pollution and climate change [1–4], renewable energy technologies that harness resources such as solar [5], wind [6, 7], and hydrogen [8] have emerged as key alternatives [2]. Consequently, demand has been growing for the large-scale production of various energy conversion and storage devices—including solar cells [9, 10], water electrolyzers [11, 12], fuel cells [13, 14], and capacitors [15, 16]—that can efficiently convert and store these forms of energy [17]. Among these, water electrolysis is particularly

Joon-Young Park and Kyeong-Rim Yeo contributed equally to this work.

This is an open access article under the terms of the Creative Commons Attribution License, which permits use, distribution and reproduction in any medium, provided the original work is properly cited.

Copyright © 2026 Joon-Young Park et al. *International Journal of Energy Research* published by John Wiley & Sons Ltd.

attractive for large-scale hydrogen production, as it generates high-purity hydrogen from water and electricity without CO_2 emissions. It is also readily scalable and can be integrated with intermittent renewable energy, making it well-suited for grid balancing and energy storage [11, 18, 19].

Despite extensive research on high-efficiency, durable, and high-performance electrodes for water electrolysis, most advancements remain confined to the laboratory scale. For the practical commercialization of eco-friendly energy conversion and storage devices, both technological performance and cost-effectiveness must be addressed. This creates an urgent need for scalable, large-area fabrication processes for water electrolysis electrodes, which are critical components of these systems [20–23].

Currently, the most widely used method for fabricating electrodes in electrochemical energy conversion systems, such as fuel cells and water electrolyzers, involves coating a conductive substrate with a composite mixture of catalyst powders, binders, and conductive additives. However, this approach presents several structural and electrical drawbacks. First, weak adhesion between the catalyst layer and substrate compromises the long-term durability of the electrode [24]. Second, the presence of binders and additives may negatively affect electrical contact within the electrode, resulting in increased resistance and lower electrochemical performance [25–27]. Third, binders often occlude or deactivate active sites, thereby limiting their direct participation in electrochemical reactions and reducing efficiency [28]. Finally, the multistep nature of this fabrication process is inherently disadvantageous in terms of manufacturing time and cost [29].

By contrast, self-supported electrode fabrication methods—where electroactive materials are directly grown onto conductive substrates—offer significant benefits by eliminating the need for binders and conductive additives, thereby lowering interfacial resistance and manufacturing costs [25, 30, 31]. Representative self-supported fabrication techniques include electrospinning [32–35], chemical vapor deposition (CVD) [36, 37], and electrodeposition [38, 39]. Electrospinning offers a facile and scalable fabrication process, tunable fiber dimensions, high specific surface area, and inherently porous nanofiber architectures. However, its practical scalability is limited by issues such as nonuniform flow distribution across multiple jets, system complexity, solvent volatility, and considerable economic and environmental costs [32, 33]. Furthermore, CVD enables uniform large-area coatings and strong adhesion between the substrate and catalyst layer but is hindered by the use of complex and often hazardous precursors, high operational costs, toxic byproduct generation, and restrictions on substrate selection and mechanical stability owing to high-temperature processing [40].

Among these techniques, electrodeposition stands out as a cost-effective and energy-efficient method that enables rapid electrode fabrication under ambient temperature and pressure [39, 41]. It provides precise control over electrode morphology, ranging from zero-dimensional (0D) nanoparticles to three-dimensional (3D) architectures, and allows fine-tuning of chemical composition through the systematic adjustment of deposition parameters such as deposition potential or current, electrolyte composition, and additive selection. Despite these advantages, scaling electrodeposition to large-area substrates presents challenges in achieving uniform deposition quality. As electrode area increases, nonuniform current density distribution can lead to significant variations in coating thickness and compositional homogeneity, which limit performance consistency and manufacturability [42, 43]. Electrodeposition has recently gained attention as a promising fabrication method for water electrolysis electrodes, exhibiting excellent performance in both proton exchange membrane water electrolyzers (PEMWEs) and anion exchange membrane water electrolyzers (AEMWEs) [44–52]. However, most studies are limited to laboratory-scale demonstrations, typically involving electrode areas of only a few square centimeters [53–57]. Reports on the fabrication of large-area electrodes—on the order of tens of square centimeters or more—for membrane electrode assembly (MEA) applications using electrodeposition remain scarce.

Although several studies have reported large-area electrode fabrication via electrodeposition, including the deposition of CIGS thin films, a solar cell electrode material, over an area of 80 cm^2 [58], and the fabrication of Ag gas diffusion electrodes (GDEs) for CO_2 reduction systems with areas of 25.5 cm^2 and 136 cm^2 [59], research still lacks of comprehensive and systematic understanding of the critical parameters needed to precisely control these processes. As discussed earlier, despite numerous reports on large-area electrode fabrication via electrodeposition, systematic insights into the key process parameters remain limited. Scaling high-performance and durable electrodes from laboratory-scale demonstrations to commercially viable systems requires meticulous optimization of critical material properties—including surface morphology, crystallographic structure, electronic configuration, and elemental composition—to preserve intrinsic activity.

In this context, the current study aims to scale up a multicomponent Cu–Ni–Mo catalyst, which previously demonstrated excellent hydrogen evolution reaction (HER) activity and durability in both half-cell and single-cell PEMWE systems [49], to an electrode area of 10.2 cm^2. This ternary catalyst exhibited a low overpotential of 18 mV at $-10\ mA\ cm^{-2}$ in half-cell testing and delivered high performance of $1.62\ A\ cm^{-2}$ at 1.9 V_{cell} in full-cell operation under small-area (~1 cm^2) conditions, achieving Pt-comparable HER performance and maintaining long-term operational stability in acidic media.

However, translating this promising activity from small-scale tests to larger electrode areas remains a formidable challenge, as scaling demands simultaneous control of catalyst composition, film uniformity, and electrochemical properties over an extended surface. To address this, we designed a custom electrodeposition cell with tunable interelectrode spacing and identified deposition potential, the distance between the working and counter electrodes (d_{WE-CE}), and the distance between the working and reference electrodes (d_{WE-RE}) as key control parameters for the scaling process. By systematically investigating the effects of these variables on catalyst morphology and composition, this study seeks to establish the optimal electrodeposition conditions for fabricating large-area electrodes using previously validated catalyst systems. Ultimately, this work aims to advance the fundamental understanding of scale-up strategies for nonprecious metal catalysts and lays the groundwork for the practical deployment of high-performance electrodes in commercial water electrolysis systems.

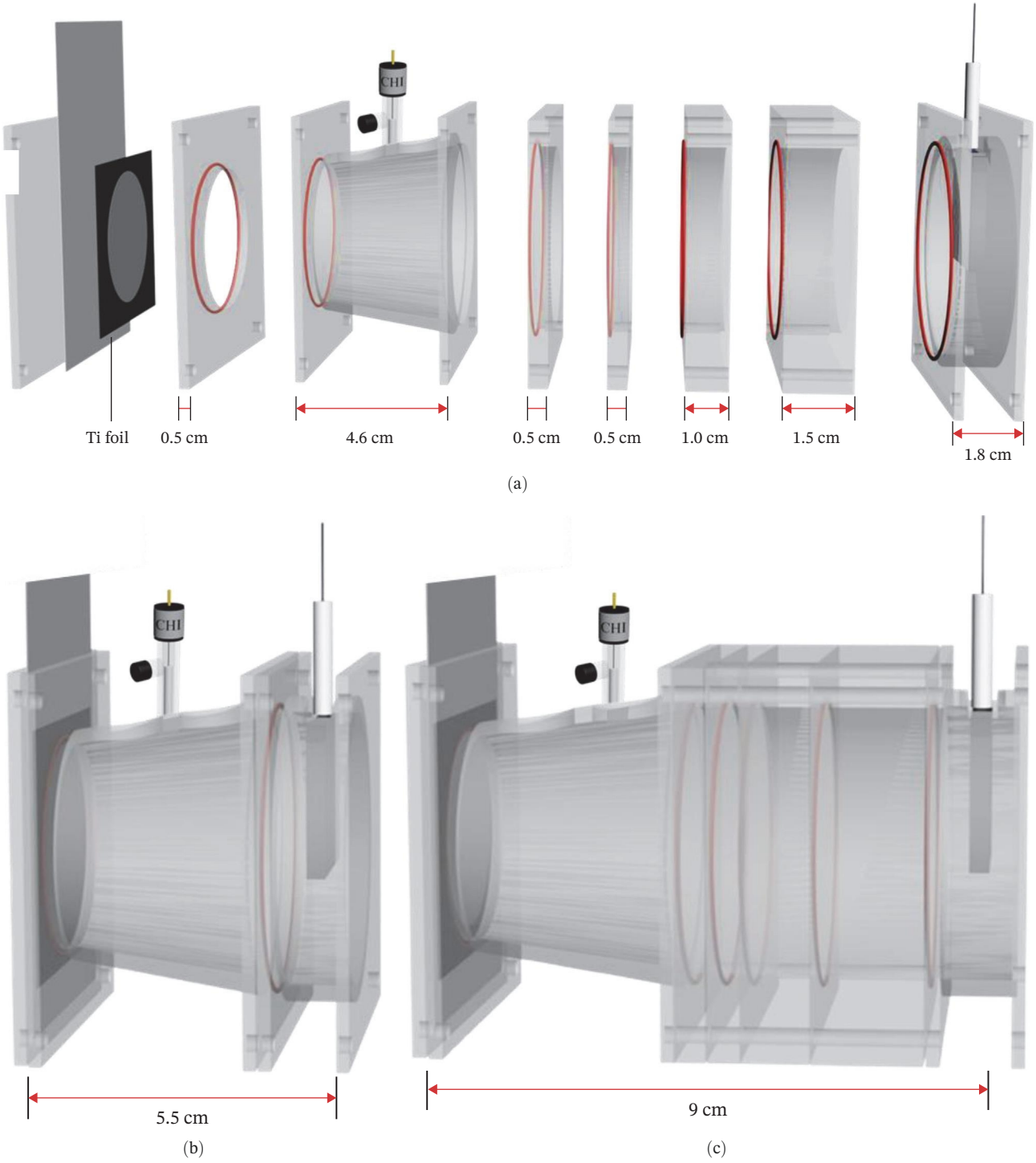
ijer, 2026, 1, Downloaded from https://onlinelibrary.wiley.com/doi/10.1155/er/5468552 by MS HYEON - Chung-Ang University , Wiley Online Library on [24/03/2026]. See the Terms and Conditions (https://onlinelibrary.wiley.com/terms-and-conditions) on Wiley Online Library for rules of use; OA articles are governed by the applicable Creative Commons License

2 | Materials and Methods

2.1 | Cell Design for Scale-Up Electrodeposition

To systematically analyze the electrochemical and physical factors influencing deposition uniformity, experiments varied three parameters independently: (1) deposition potential, (2) d_{WE-CE}, and (3) d_{WE-RE}. A custom-designed polycarbonate electrodeposition cell was fabricated, as illustrated in Scheme 1a. The basic configuration of the cell consisted of a carbon paper as the WE, Ti foil placed behind the carbon paper as the electric lead, an endplate for cell assembly, and fixtures to secure the RE and CE.

To investigate the effect of interelectrode spacing on catalyst deposition patterns, spacers with thicknesses of 0.5 (×2), 1.0, and 1.5 cm were fabricated for insertion between the WE and CE. Additionally, a separate 0.5 cm spacer was produced for positioning between the WE and RE. As shown in Supporting Information Scheme S1a,b, the reference electrode fixture contained



SCHEME 1 | (a) Schematic of the electrodeposition cell for fabricating a scaled-up (10.2 cm²) electrocatalyst. Cell configuration with the (b) shortest d_{WE-CE} and (c) maximum d_{WE-CE}.

ijer, 2026, 1, Downloaded from https://onlinelibrary.wiley.com/doi/10.1155/er/5468552 by MS HYEON - Chung-Ang University , Wiley Online Library on [24/03/2026]. See the Terms and Conditions (https://onlinelibrary.wiley.com/terms-and-conditions) on Wiley Online Library for rules of use; OA articles are governed by the applicable Creative Commons License

two 15 mm holes for securing the reference electrode and allowing the adjustment of the d_{WE-RE} to 1.45 and 3.15 cm. Furthermore, by inserting a 0.5 cm spacer between the endplate and RE fixture, the d_{WE-RE} could be extended by 0.5 cm beyond these values, enabling comparison across four discrete distances: 1.45, 1.95, 3.15, and 3.65 cm.

As shown in Scheme 1b, the minimum d_{WE-CE} achievable in the standard cell configuration was 5.5 cm, while the maximum, shown in Scheme 1c, was 9 cm. For catalyst fabrication over an enlarged 50 cm^2 area, an additional electrodeposition cell with a similar design but larger scale was constructed, maintaining d_{WE-RE} at 1.15 cm and d_{WE-CE} at 5.0 cm.

2.2 | Fabrication of Cu–Ni–Mo Electrode

To enable the scale-up production of Cu–Ni–Mo ternary alloy electrode catalysts, an electrodeposition method was employed using a three-electrode configuration. A 10.2 cm^2 carbon paper (Ballard, Avcarb MGL280) served as the WE, a saturated calomel electrode (SCE; CHI 150) served as the RE, and a rectangular graphite plate with dimensions of $2.3 \times 3.0 \times 0.3$ cm^3 served as the CE. Although only one face of the CE directly faced the WE, multiple surfaces of the graphite plate were exposed to the electrolyte, providing a sufficient effective electrochemically accessible surface area. The electrolyte composition, following the optimized formulation from prior research [49], consisted of 0.03 M $CuSO_4 \cdot 5H_2O$ (Daejung, 2588-4400), 0.25M $C_6H_5Na_3O_7 \cdot 2H_2O$ (Na_3Cit, Daejung, 7555-4405), 0.1M $Na_2MoO_4 \cdot 2H_2O$ (Daejung, 7598-4405), and 0.3M $NiSO_4 \cdot 6H_2O$ (Daejung, 5611-4400). Electrodeposition was performed using a potentiostat (CS350, Wuhan CorrTest Instrument Corp., Ltd), with deposition potential and interelectrode distances (d_{WE-CE} and d_{WE-RE}) independently controlled, while deposition time remained fixed at 600 s. The electrodeposition was conducted without stirring, and the applied potential during the deposition process was not iR-compensated. Detailed electrodeposition parameters are presented in Table 1.

The optimized electrodeposition protocol for the 10.2 cm^2 electrode was applied to a similarly fabricated 50 cm^2 electrode to verify scalability. A 50 cm^2 carbon paper and a 5.0×5.0 cm graphite plate served as WE and CE, respectively, and electrodeposition was performed at a deposition potential of −1.8 V_{SCE} for 600 s.

2.3 | Electrochemical Characterization

To evaluate the electrochemical uniformity of the fabricated catalyst, small-area electrodes were cut from four different positions within the 10.2 cm^2 electrode, as shown in Supporting Information Scheme S2a. Electrochemical measurements were conducted using a custom-made Teflon cell with an exposed area of 1.43 cm^2. All experiments were conducted at ambient temperature and pressure in a 0.5 M H_2SO_4 electrolyte. A graphite rod served as the CE.

The HER activity was evaluated using cyclic voltammetry (CV) over a potential range from 0.02 to −0.23 V_{RHE} with a scan rate of 1 mV s^{-1}. All applied potentials were iR-compensated and converted to the reversible hydrogen electrode (RHE) scale using the following equation:

TABLE 1 | Electrodeposition conditions under varying deposition potentials, d_{WE-CE}, and d_{WE-RE}.

Variation case	Deposition potential/V_{SCE}	WE–RE/cm	WE–CE/cm
Variation 1	−1.5	1.45	5.5
	−1.8		
	−1.9		
	−1.95		
	−2		
	−2.3		
	−2.5		
Variation 2	−1.95	1.45	5.5
			6
			6.5
			7
			7.5
			8
			8.5
			9
Variation 3	−1.95	1.45	5.5
		1.95	
		3.15	
		3.65	

$$E_{RHE} = E_{exp} + E_{ref} + 0.0592\,V \times pH\ . \quad (1)$$

Solution resistance (R_s) as a function of interelectrode distance was measured by electrochemical impedance spectroscopy (EIS) using a potentiostat at a DC potential of 0.37 V_{RHE}, with an AC signal amplitude of 10 mV over a frequency range of 10^5 to 10^{-1} Hz. The 50 cm^2 scaled-up electrode was also evaluated for HER activity using CV measurements under identical conditions at nine different locations, as shown in Supporting Information Scheme S2b.

2.4 | Physicochemical Characterization

Surface morphology was characterized using field-emission scanning electron microscopy (FE-SEM; Carl Zeiss, SIGMA), and the elemental composition of the electrodeposited catalysts was analyzed using energy-dispersive X-ray spectroscopy (EDS; Thermo Fisher, NORAN System 7). Morphological and compositional analyses accompanied the electrochemical measurements at four different positions to assess deposition uniformity across the electrode surface. For catalysts prepared under optimized conditions, crystallographic analysis was performed using X-ray diffraction (XRD; Bruker-AXS, NEW D8-Advance). Diffraction patterns were recorded over a 2θ range of 30° to 80° at a scan rate of 5° min^{-1}, and the resulting data were compared with those of the reference catalyst to verify phase consistency. In addition, to enable a direct comparison of diffraction peak positions as a function of deposition potential, XRD patterns of catalysts deposited across the entire potential range were measured at position 1 as defined in Supporting Information Scheme S2a using an identical 2θ range but with a reduced scan rate of 1.7° min^{-1}. This

ijer, 2026, 1, Downloaded from https://onlinelibrary.wiley.com/doi/10.1155/er/5468552 by MS HYEON - Chung-Ang University , Wiley Online Library on [24/03/2026]. See the Terms and Conditions (https://onlinelibrary.wiley.com/terms-and-conditions) on Wiley Online Library for rules of use; OA articles are governed by the applicable Creative Commons License

improved angular resolution allowed subtle peak shifts associated with compositional variations to be more clearly resolved.

2.5 | Single-Cell Operation

A 50.8-μm-thick Nafion 212 membrane (DuPont) served as the proton exchange membrane. The anode consisted of IrO_2 (loading: 0.1 mg cm^{-2}) deposited on carbon paper [60]. The cathode consisted of the fabricated 10.2 cm^2 large-area catalyst-deposited electrode (Supporting Information Scheme S2c) under the optimized deposition condition, divided into four equal sections (Supporting Information Scheme S2a), with each section evaluated individually. The MEA area was 1 cm^2, and the cell operating temperature was maintained at 90°C. Deionized water, used as the reactant, was fed to the anode side at a 15 mL min^{-1} flow rate. Before performance testing, the cell underwent an initial activation step involving the application of 2.3 V_{cell} for 30 min. Electrochemical performance of the PEMWE system was then evaluated by stepwise variation of the current density from 4 to 0.02 A cm^{-2} at 1 min intervals.

3 | Results and Discussion

3.1 | Effect of Deposition Potential

In constant-potential electrodeposition, the deposition potential modulates the reduction current density and deposition rate, thereby influencing ionic transport within the electrolyte as well as nucleation and growth of catalyst particles [39, 61–64]. As such, it serves as a crucial parameter that directly governs key catalyst properties, including alloy composition, surface morphology, crystallinity, and electronic structure [39, 61, 65]. Therefore, experiments varied the deposition potential as a variable to elucidate its impact on the deposition process and identify the optimal conditions for scale-up of the target catalyst. In these experiments, $d_{WE–CE}$ was fixed at 5.5 cm, while $d_{WE–RE}$ was maintained at 1.45 cm. Deposition was conducted under seven different deposition potentials, ranging from −1.5 V_{SCE}, the value used in our previous work [49], to −2.5 V_{SCE}, with different intervals ranging from 0.05 V_{SCE} to 0.3 V_{SCE}.

Supporting Information Figure S1a illustrates *i–t* curves showing the deposition current density at different deposition potentials, where increasingly negative deposition potentials produced higher deposition current densities. The enhanced saw-tooth current behavior at more negative potentials reflects the increasing influence of concurrent hydrogen evolution during electrodeposition. EDS analysis examined how changes in reduction current density affected the composition. Figure 1 presents the plots with average values obtained from four different positions, along with standard deviations shown as error bars. When plotting the average elemental compositions of each NiMoCu component obtained from four positions, as shown in Figure 1a, Mo content varied little with changes in deposition potential, averaging 8.5%–10.8%. However, Ni and Cu exhibited greater compositional changes influenced by deposition potential, ranging from 39.1% to 49.5% and 40.5% to 51%, respectively. Furthermore, analysis of the compositional standard deviations at different positions for catalysts electrodeposited under all deposition potentials revealed maximum variations of 2.1%, 1.8%, and 0.4% for Cu, Ni, and Mo, respectively.

As seen in Figure 1a, at a deposition potential of −1.5 V_{SCE}, the composition of the catalyst deposited over a 10.2 cm^2 area differed from that of the catalyst prepared on a 1.43 cm^2 area under identical conditions in our previous study [49], namely, $Cu_{44.4}Ni_{46}Mo_{9.6}$ (hereafter referred to as the reference sample). For the large-area electrodeposited catalyst, the Cu content was slightly higher, while the Ni content was somewhat lower compared to the reference sample, and this trend persisted as the deposition potential increased up to −1.9 V_{SCE}. The differences in alloy composition between the reference sample and the 10.2 cm^2 sample deposited at −1.5 V_{SCE} were likely due to variations in the electrodeposition cell design. Key differences include the use of different counter electrode geometries (graphite rod vs. graphite plate), distinct electrode arrangements (perpendicular vs. parallel configuration), and variations in electrolyte volume (~30 cm^3 vs. 73 cm^3). These design differences could have affected local current distribution, mass transport, and potential gradients, thereby influencing the relative deposition rates of Cu and Ni.

However, as the deposition potential became more negative, the amount of Ni deposited gradually increased. At potentials more negative than −1.95 V_{SCE}, the Ni content exceeded the Cu content, and this difference progressively increased. When coelectrodepositing Ni and Cu from a single electrolyte, the deposition potential plays a critical role in determining the final alloy composition due to the significant difference in their standard reduction potentials (Cu^{2+}/Cu: +0.34 V; Ni^{2+}/Ni: −0.25 V_{SHE}). At relatively less negative potentials, such as −1.5 V_{SCE}, Cu, with a more positive standard reduction potential, was preferentially reduced and deposited, producing an alloy richer in Cu and lower in Ni. As the deposition potential became more negative, the overpotential increased more substantially for Ni^{2+} reduction than for Cu^{2+} reduction due to the larger relative thermodynamic gap between the deposition potential and the standard reduction potential of Ni. This led to a higher rate of Ni incorporation into the deposit, raising the Ni content while decreasing the relative Cu content. This compositional shift with increasing negative potential is characteristic of kinetically controlled alloy electrodeposition systems and reflects the interplay between thermodynamic reduction tendencies and mass transport limitations in the electrolyte [66]. Unlike Cu and Ni, Mo did not electrodeposit through the direct reduction of its single metal ions but required the formation of appropriate complexes with metal ions and citrate for reduction [67]. Consequently, Mo electrodeposition relied on an induced codeposition mechanism [68–70], making its composition relatively less sensitive to changes in the deposition potential.

Notably, as shown in Figure 1b, which shows the average of absolute values of the compositional differences for each element with respect to the reference sample at various deposition potentials, the catalyst electrodeposited at −1.95 V_{SCE} exhibited an average composition ($Cu_{44.3}Ni_{44.9}Mo_{10.8}$) closest to that of the reference sample ($Cu_{44.4}Ni_{46}Mo_{9.6}$). Figure 1c, which presents the average overpotentials at −10 mA cm^{-2} for the HER activity of electrodes deposited under different deposition potentials, further revealed that deposition at −1.95 V_{SCE} yielded an overpotential of 17.8 mV, nearly identical to that of the reference sample (18 mV). The HER polarization curves for each deposition potential are provided in Supporting Information Figure S1b–h.

ijer, 2026, 1, Downloaded from https://onlinelibrary.wiley.com/doi/10.1155/er/5468552 by MS HYEON - Chung-Ang University , Wiley Online Library on [24/03/2026]. See the Terms and Conditions (https://onlinelibrary.wiley.com/terms-and-conditions) on Wiley Online Library for rules of use; OA articles are governed by the applicable Creative Commons License

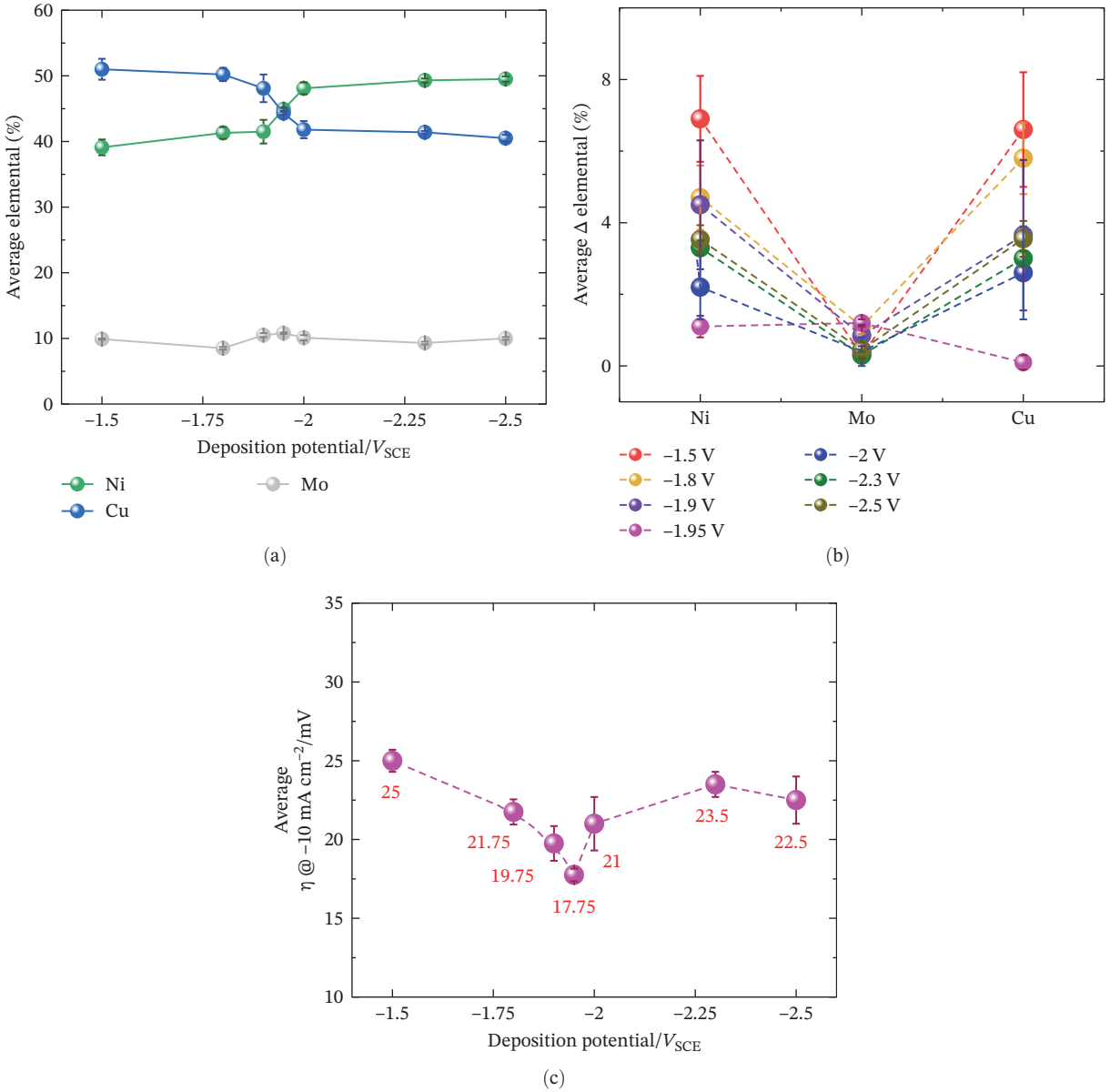


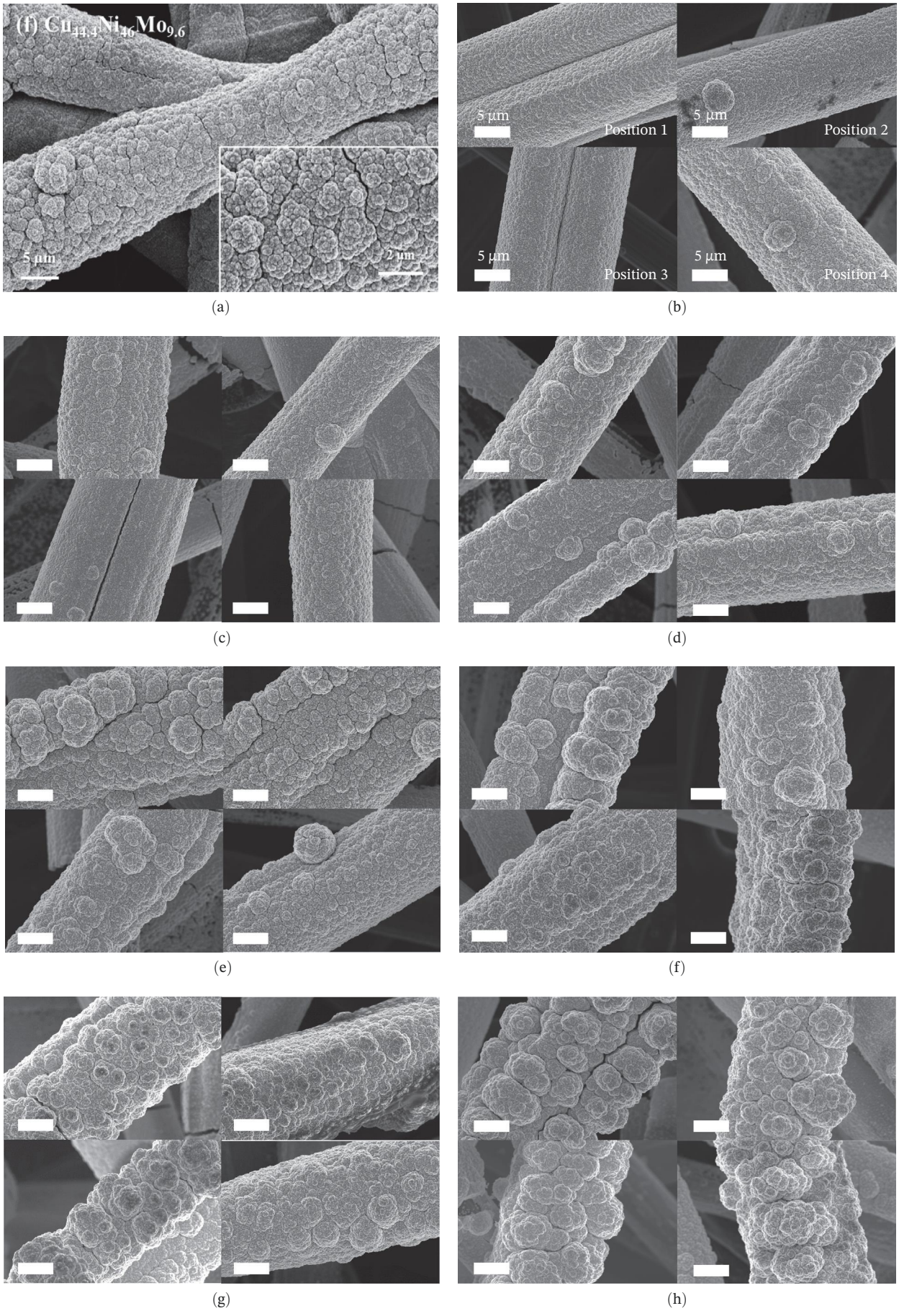
FIGURE 1 | Average (a) elemental %, (b) Δ elemental % from FE-SEM EDS, and (c) η (mV) at −10 mA cm^{-2} measured at four positions of the scaled-up catalyst under different deposition potentials.

Deviations from −1.95 V_{SCE} produced larger compositional differences, accompanied by corresponding changes in HER activity. This demonstrates that compositional control is critical for achieving high performance when fabricating large-area electrodes.

Figure 2a shows the FE-SEM micrograph of the reference sample [49], while Figure 2b–h shows those of the catalysts electrodeposited over a 10.2 cm^2 area at deposition potentials ranging from −1.5 V_{SCE} to −2.5 V_{SCE}. The micrographs in Figure 2b–h, each divided into four quadrants, were taken from the positions indicated in Supporting Information Scheme S2a. The morphological evolution with increasingly negative potential revealed distinct trends in particle distribution, size, and surface coverage. Notably, the morphologies observed at −1.95 V_{SCE} (Figure 2e) and −2.0 V_{SCE} (Figure 2f) most closely resembled that of the reference sample shown in Figure 2a. These samples exhibited similar particle coverage across the fibrous surfaces, along with comparable particle size and spacing. These similarities indicate that deposition at −1.95 V_{SCE}–−2.0 V_{SCE} produced nucleation and growth behavior closely matching those from the original reference conditions in the smaller-scale Teflon cell. By contrast, deposition at more positive (−1.5 V_{SCE}; Figure 2b) or more negative potentials (−2.3 and −2.5 V_{SCE}; Figure 2g–h) led to morphological deviations likely caused by differences in reduction kinetics and mass transport conditions. Regardless of the deposition potential, the catalyst morphologies at different positions on each sample remained relatively similar, indicating uniform electrodeposition across the 10.2 cm^2 electrode. Together with the observed similarities in compositional and electrochemical results, the morphological match at −1.95 V_{SCE} further confirms that this condition best reproduced the characteristics of the reference catalyst under scaled-up conditions.

XRD analysis at four positions of the catalyst electrodeposited at −1.95 V_{SCE} (Figure 3) revealed distinct CuNi alloy peaks, slightly

ijer, 2026, 1, Downloaded from https://onlinelibrary.wiley.com/doi/10.1155/er/5468552 by MS HYEON - Chung-Ang University , Wiley Online Library on [24/03/2026]. See the Terms and Conditions (https://onlinelibrary.wiley.com/terms-and-conditions) on Wiley Online Library for rules of use; OA articles are governed by the applicable Creative Commons License



ijer, 2026, 1, Downloaded from https://onlinelibrary.wiley.com/doi/10.1155/er/5468552 by MS HYEON - Chung-Ang University , Wiley Online Library on [24/03/2026]. See the Terms and Conditions (https://onlinelibrary.wiley.com/terms-and-conditions) on Wiley Online Library for rules of use; OA articles are governed by the applicable Creative Commons License

broadened owing to Mo incorporation. Since the Mo content remained below 10%, the catalysts retained relatively good crystallinity with clearly visible peaks, consistent with our previous findings [49]. Moreover, the similarity in peak positions across different locations indicates uniform structural characteristics across the entire electrode surface. Following the compositional trends identified by EDS analysis (Figure 1a), the crystallographic features of the catalysts deposited at different potentials were further examined by XRD. As shown in Supporting Information Figure S2, all samples exhibit characteristic diffraction peaks corresponding to a CuNi solid solution, confirming successful alloy formation over the entire deposition potential range. Consistent with the EDS results, the Mo content remained below 10 at% for all samples, leading to only slight peak broadening without the appearance of secondary Mo-related phases. At deposition potentials from −1.5 to −1.9 V_{SCE}, where EDS reveals Cu-rich compositions, the alloy diffraction peaks are shifted toward lower 2θ values, closer to those of metallic Cu. In contrast, as the deposition potential becomes more negative (−1.95 to −2.5 V_{SCE}), corresponding to Ni-rich compositions, the diffraction peaks shift toward higher 2θ values and become sharper. This peak shift directly reflects composition-dependent changes in the lattice parameter of the CuNi alloy, in good agreement with Vegard's law [62, 71], and further corroborates the compositional evolution inferred from EDS analysis.

3.2 | Effect of Distance Between Working and Counter Electrodes

Variations in d_{WE-CE} can influence the electrodeposition process by modifying the local ionic environment. Such variations may affect current distribution, concentration gradients, and electrolyte flow dynamics near the electrode surface, affecting the uniformity of ion supply and the resulting alloy composition, surface morphology, and crystal growth behavior of the deposited catalyst [72–75]. Accordingly, to investigate the effect of d_{WE-CE} variation on the deposition process and catalyst properties, the d_{WE-RE} was fixed at 1.45 cm, and the optimized deposition potential of −1.95 V_{SCE} was applied. The d_{WE-CE} was adjusted incrementally from 5.5 to 9 cm. The change in deposition charge with varying d_{WE-CE} was analyzed by integrating the *i*–*t* curves (Supporting Information Figure S3a), with the results shown in Supporting Information Figure S3b. The total charge under each d_{WE-CE} condition remained comparable, ranging from 17 C to 16.2 C cm^{-2}. This consistency indicates that the parallel arrangement of the WE and CE in the electrodeposition setup reduced the impact of d_{WE-CE} on the overall current flow.

Based on observations from FE-SEM images (Figure 2e and Supporting Information Figure S4), at a short d_{WE-CE} of 5.5 cm (Figure 2e), relatively large spherical particles were densely distributed, exhibiting an aggregated form with distinct boundaries that were observed at all positions. Within 6–7 cm (Supporting Information Figure S4a,b), the particle size and density remained relatively uniform across positions, and the surface maintained a dense and flat morphology. Beyond 8 cm (Supporting Information Figure S4c,d), the surface density and flat morphology were preserved, but noticeable differences in surface structure appeared depending on the position.

Figure 4a shows the variation in average elemental composition, measured from four different sample positions, with d_{WE-CE}. The error bars indicate the standard deviation from these four positions. As d_{WE-CE} increased from 5.5 to 9 cm, Ni content slightly increased from 44.9% to 47%. Conversely, the Cu content increased modestly from 44.3% to 45% when the distance increased from 5.5 to 6 cm and then declined to 43.1% at 9 cm. Compared to Ni and Cu, the Mo content slightly varied from 8.7% to 10.8% without a clear trend relative to interelectrode distance.

Variations in d_{WE-CE} influence the electrochemical deposition environment by altering the electric field distribution and ion transport dynamics [73, 75]. Although ions can diffuse toward the WE from multiple directions, changes in d_{WE-CE} affect the dominant migration pathways and local ion concentrations near the electrode surface [75]. This effect is particularly significant for diffusion-limited species like Cu^{2+}, whereas more abundant ions such as Ni^{2+} are less affected [72, 76]. Consequently, the deposited alloy composition can shift due to the combined effects of electric field variation and species-specific mass transport [72, 74, 75]. Additionally, for all d_{WE-CE} conditions, the composition standard deviations across positions were limited to 1.8% for Cu, 1.3% for Ni, and 0.8% for Mo, indicating high deposition uniformity.

HER activity (Figure 4b) also varied with changes in d_{WE-CE}. The average overpotential at −10 mA cm^{-2}, measured from four different positions of each electrode (Supporting Information Figure S5), increased with d_{WE-CE}. Notably, the sample prepared at 5.5 cm, which had a composition closest to that of the reference sample, exhibited the lowest overpotential. This result suggests that increasing d_{WE-CE} altered the alloy composition through changes in ion transport conditions, thereby negatively impacting catalytic performance by deviating from the optimal composition.

In conclusion, although the total charges passed remained comparable with variations in d_{WE-CE}, FE-SEM observations revealed that particle size and distribution uniformity depended on the interelectrode distance. At 5.5 cm, densely packed spherical particles were formed uniformly, whereas increasing the distance produced more pronounced positional differences in surface morphology. Compositional analysis showed minor variations in Ni and Cu content with changing distance, whereas Mo content exhibited no clear trend. Furthermore, the overpotential for the HER increased with d_{WE-CE}, indicating that variations in electrode spacing affect ion transport and compositional distribution, thereby impacting catalytic activity. These findings underscore the critical importance of optimizing d_{WE-CE} to achieve superior catalytic performance.

FIGURE 2 | (a) FE-SEM micrographs of the reference catalyst deposited at −1.5 V_{SCE}, reproduced with permission from Ref. [49]. Copyright 2021 Elsevier. FE-SEM images of the scaled-up electrocatalysts at four positions under different deposition potentials: (b) −1.5, (c) −1.8, (d) −1.9, (e) −1.95, (f) −2, (g) −2.3, and (h) −2.5 V_{SCE}.

ijer, 2026, 1, Downloaded from https://onlinelibrary.wiley.com/doi/10.1155/er/5468552 by MS HYEON - Chung-Ang University , Wiley Online Library on [24/03/2026]. See the Terms and Conditions (https://onlinelibrary.wiley.com/terms-and-conditions) on Wiley Online Library for rules of use; OA articles are governed by the applicable Creative Commons License

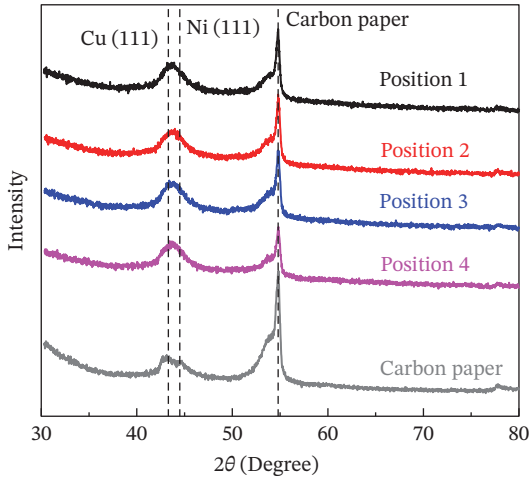


FIGURE 3 | XRD patterns of carbon paper and four positions of the scaled-up catalyst deposited at −1.95 V_{SCE}.

3.3 | Effect of Distance Between Working and Reference Electrodes

In electrodeposition processes, d_{WE-RE} serves as a critical parameter directly affecting the accuracy of the potential applied to the WE. As d_{WE-RE} increases, the solution resistance also increases, thereby amplifying the discrepancy between the potential measured by the RE and the actual potential experienced at the WE surface [77]. To investigate how variations in d_{WE-RE} influence the electrochemical and physicochemical properties of the electrode during large-area deposition, a series of controlled experiments was conducted. Based on prior results, the d_{WE-CE} was fixed at 5.5 cm, and the deposition potential was maintained at −1.95 V_{SCE}. Electrodeposition was then performed at d_{WE-RE} values of 1.45, 1.95, 3.15, and 3.65 cm.

As illustrated in Supporting Information Figure S6a, the deposition current density decreased significantly with increasing d_{WE-RE}, in contrast to the relatively small differences observed when varying d_{WE-CE} (Supporting Information Figure S3a). This decline was closely linked to the rise in solution resistance, which, as shown in Figure 5a, increased nearly linearly from 18.4 to 67.3 $\Omega\,cm^2$ as d_{WE-RE} increased from 1.45 to 3.65 cm. The increased solution resistance induced a larger voltage drop across the electrolyte, reducing the actual potential at the WE surface compared to the set value, thereby suppressing the reduction kinetics of metal ions.

These electrochemical shifts were reflected in the surface morphology and compositional evolution of the electrodeposited catalyst, as confirmed by FE-SEM (Supporting Information Figure S7) and EDS (Figure 5b). As shown in Figure 2e, the catalyst deposited at a d_{WE-RE} of 1.45 cm exhibited well-developed spherical grains uniformly distributed over the surface, correlating with the highest observed electrochemical performance. This is attributed to the minimal ohmic drop, resulting in a sufficiently negative actual deposition potential. However, as d_{WE-RE} increased, the higher solution resistance led to a noticeable decrease in the actual deposition potential, even when the deposition potential was fixed at −1.95 V_{SCE}. Consequently, the surface morphology shifted toward less developed structures (Supporting Information Figure S7a–c), similar to those obtained at lower deposition potentials of −1.5 or −1.8 V_{SCE} (Figure 2b,c). This indicates that d_{WE-RE} directly modulated the local electrochemical environment and nucleation and growth behaviors during electrodeposition.

The EDS data in Figure 5b represent the average elemental composition obtained from four distinct positions on each sample to ensure representative analysis. The error bars in Figure 5 indicate the standard deviation calculated from measurements at these locations, consistent with the method used in Figures 1 and 4. As d_{WE-RE} increased, the Cu content increased significantly from 44.3% (1.45 cm) to 79.6% (3.65 cm), while Ni content decreased accordingly from 44.9% to 15.8%. The Mo content gradually

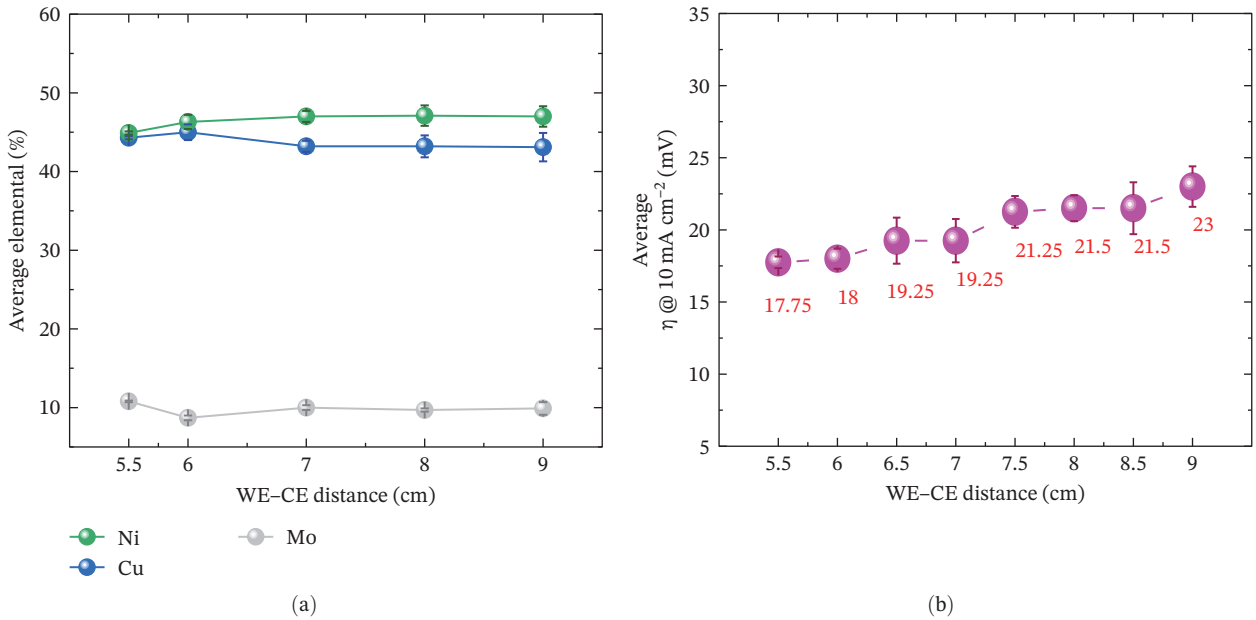


FIGURE 4 | Average (a) elemental % from FE-SEM EDS and (b) η (mV) at −10 mA cm^{-2} measured at four positions of the scaled-up catalyst under different d_{WE-CE}.

ijer, 2026, 1, Downloaded from https://onlinelibrary.wiley.com/doi/10.1155/er/5468552 by MS HYEON - Chung-Ang University , Wiley Online Library on [24/03/2026]. See the Terms and Conditions (https://onlinelibrary.wiley.com/terms-and-conditions) on Wiley Online Library for rules of use; OA articles are governed by the applicable Creative Commons License

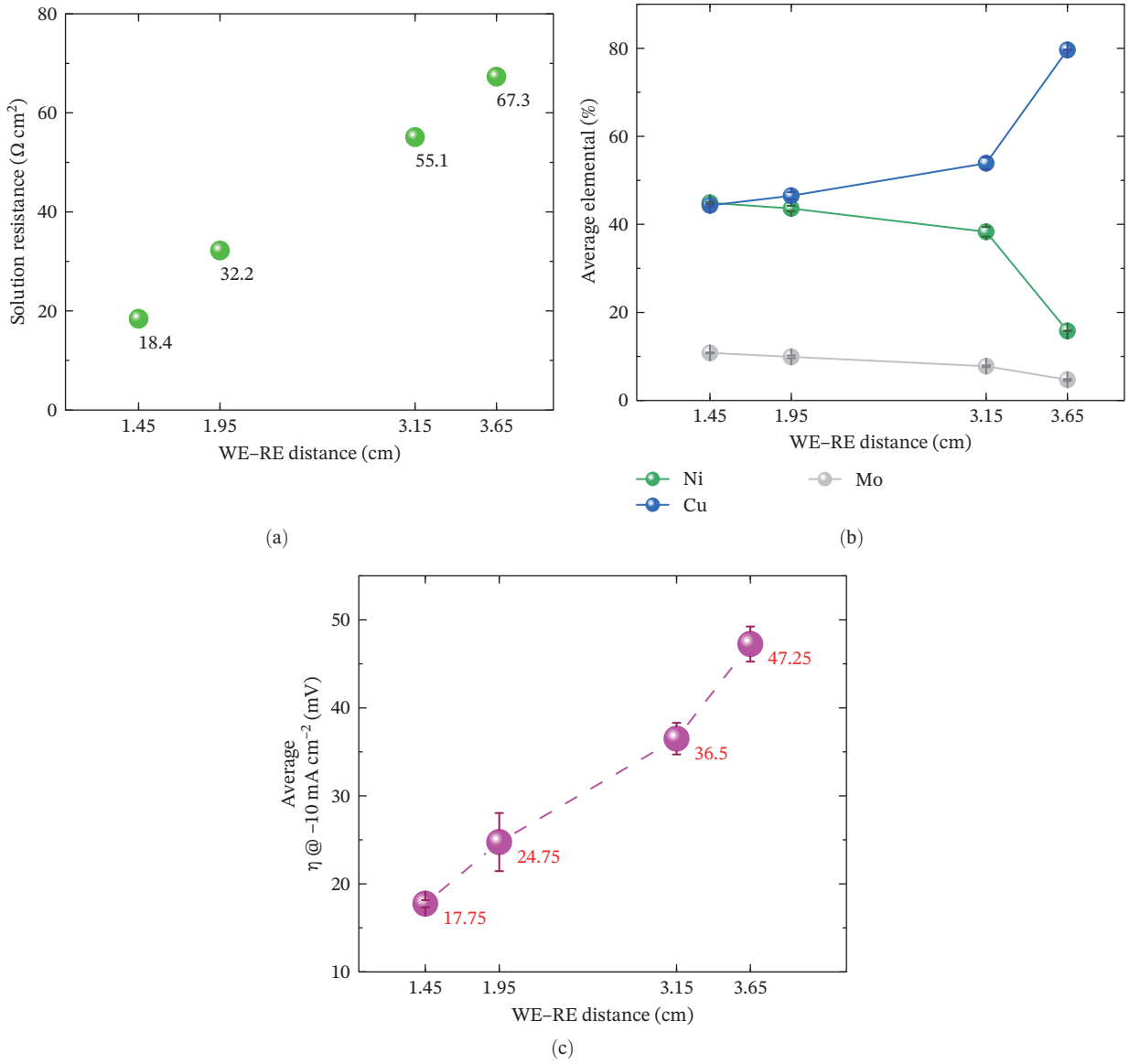


FIGURE 5 | (a) Solution resistance, (b) average elemental % from FE-SEM EDS, and (c) average η (mV) at $-10\,mA\,cm^{-2}$ measured at four positions of the scaled-up catalyst under different d_{WE-RE}.

declined with increasing d_{WE-RE}, with a relatively abrupt drop observed at 3.65 cm. This compositional shift suggests that as the effective overpotential for deposition decreased due to increased solution resistance, the reduction of less noble metals such as Ni became kinetically less favorable compared to that of more noble metals like Cu, leading to preferential Cu deposition at larger d_{WE-RE}. This observation is consistent with previous studies on Ni–Cu and Cu–Ni–Mo alloy plating [62–64, 72], which reported that reduced deposition current density due to increased d_{WE-RE} promotes Cu deposition, while comparatively suppressing the reduction of Ni and Mo. These findings underscore the critical influence of d_{WE-RE} on both the electrochemical behavior and composition of the deposited catalyst, highlighting the need for careful optimization of this parameter in scaled-up electrodeposition systems. Notably, despite variations in d_{WE-RE}, the catalysts exhibited excellent compositional uniformity across different positions, with standard deviations of only 1.3%, 1.1%, and 0.3% for Cu, Ni, and Mo, respectively.

Figure 5c shows the average HER overpotential measured at $-10\,mA\,cm^{-2}$ as a function of d_{WE-RE}. The plotted values are the average of four measurements taken at different positions on each sample to ensure reliability and account for local variation. The corresponding HER polarization curves are presented in Supporting Information Figure S6b–d. A clear linear correlation was observed: as d_{WE-RE} increased from 1.45 to 3.65 cm, the overpotential increased from 17.75 to 47.25 mV. This trend is attributed to compositional and morphological changes in the deposited catalyst layer caused by variations in the actual deposition potential, as shown in Figure 5b.

In conclusion, d_{WE-RE} proved to be a critical parameter influencing the electrodeposition process, affecting not only the catalyst composition and surface morphology but also the HER performance. As the distance increased, a greater discrepancy developed between the set potential and the actual potential experienced at the WE, effectively modulating the true deposition

ijer, 2026, 1, Downloaded from https://onlinelibrary.wiley.com/doi/10.1155/er/5468552 by MS HYEON - Chung-Ang University , Wiley Online Library on [24/03/2026]. See the Terms and Conditions (https://onlinelibrary.wiley.com/terms-and-conditions) on Wiley Online Library for rules of use; OA articles are governed by the applicable Creative Commons License

potential [77, 78]. This shift led to pronounced changes in elemental composition, surface morphology, and catalytic behavior. Therefore, precise control of d_{WE-RE} is essential under constant-potential deposition conditions to ensure process reproducibility and maximize HER catalytic activity.

Building on our understanding of the key scale-up parameters in electrodeposition, we designed a custom cell for fabricating a 50 cm^2 electrode. The objective was to replicate the properties of the reference sample by strictly following the established deposition protocol. To assess uniformity, the fabricated 50 cm^2 catalyst was divided into nine sections (Supporting Information Scheme S2b), and the HER performance in each location was evaluated (Supporting Information Figure S8). A photograph of the deposited catalyst is provided in Supporting Information Scheme S2d. The average overpotential at −10 mA cm^{-2} across positions 1–9 was 18.3 mV, remarkably close to the 18 mV recorded for the reference sample. Additionally, the minimal standard deviation of 0.8 mV among the nine regions clearly confirms the high uniformity and reproducibility of the large-area electrode. These results establish a robust and scalable methodology for fabricating highly uniform electrodes, which is critical for industrial-scale electrochemical applications.

3.4 | Single-Cell Operation

The electrode was fabricated using a custom-designed cell for 10.2 cm^2 area deposition, under deposition conditions optimized in this study (−1.95 V_{SCE}, d_{WE-CE}: 5.5 cm, d_{WE-RE}: 1.45 cm) to produce a catalyst with physicochemical and electrochemical properties closely matching those of the small-area reference sample. As presented in Figure 6, the performance of the fabricated large-area electrode was evaluated by dividing it into four smaller electrodes, each tested as the cathode in a PEMWE system. At a 1 A cm^{-2} current density, the required cell voltages for the four subdivided electrodes were 1.88, 1.87, 1.84, and 1.82 V_{cell}. At 2 A cm^{-2}, the required voltages were 2.03, 2.01, 2.00, and 2.01 V_{cell}, respectively. The negligible variation in PEMWE performance across these four regions strongly supports the successful and uniform fabrication of the 10.2 cm^2 catalyst. However, the scaled-up catalyst exhibited slightly reduced performance compared to the reference sample (1.79 and 1.95 V_{cell} at 1 and 2 A cm^{-2} [49]). Although the PEMWE evaluation used an identical electrode area as the reference sample, the slight performance reduction in the subdivided electrodes may be attributed to subtle variations in microstructure or surface properties introduced during large-area fabrication. These differences could have stemmed from minor gradients in current density, temperature, or mass transport during electrodeposition over the larger area, potentially leading to less optimal local catalyst characteristics.

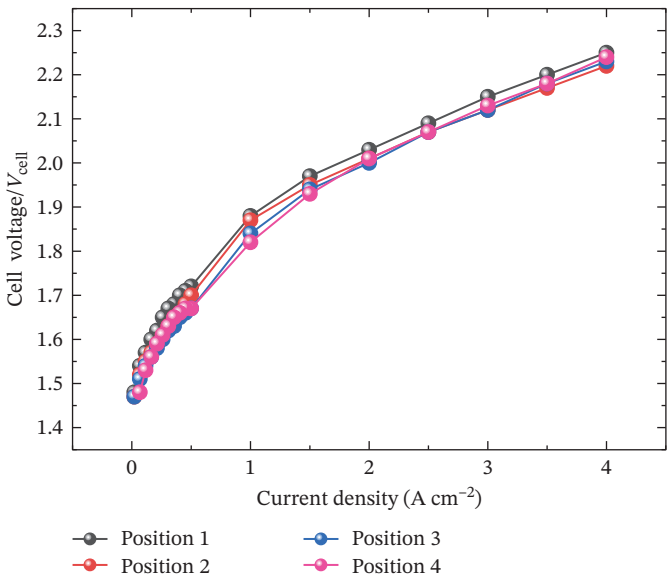


FIGURE 6 | PEMWE performances measured at different positions on a 10.2 cm^2 cathode deposited under optimized conditions (−1.95 V_{SCE}, d_{WE-CE}: 5.5 cm, and d_{WE-RE}: 1.45 cm), with IrO_2 (0.1 mg cm^{-2}) anode.

In conclusion, this study demonstrates the successful and uniform fabrication of a 10.2 cm^2 electrode with consistent PEMWE performance across the expanded active area. Despite the minor deviation from the target catalyst, these results represent a significant advance toward the scalable and practical deployment of high-performance PEMWE catalysts.

4 | Conclusions

This study presents a systematic approach for the uniform fabrication of large-area, multicomponent Cu–Ni–Mo electrodeposited catalysts for HER in PEMWE, developed from a reference catalyst that exhibited excellent performance in small-area evaluations. To reproduce the superior performance of the small-area catalyst in a larger format, key electrodeposition parameters, including deposition potential and interelectrode distances, were precisely optimized. As the electrode area increased, the deposition cell configuration and electrode arrangement were modified, requiring adjustments in deposition potential to maintain similar deposition conditions. In particular, d_{WE-RE} directly influenced the actual potential applied to the electrode, thereby significantly affecting the catalyst composition and electrochemical activity. Additionally, d_{WE-CE} influenced the deposition current density and deposition uniformity, underscoring the importance of careful electrode configuration in large-area electrode fabrication.

Through optimization of these parameters, a uniform 10.2 cm^2 electrode was successfully fabricated and subsequently divided into four smaller sections to assess uniformity by evaluating performance variations across different positions. Consequently, all subelectrodes exhibited highly consistent performance, with cell voltages ranging from 2.00 to 2.03 V_{cell} at a current density of 2 A cm^{-2}. Compared to the reference catalyst (1.95 V_{cell} at 2 A cm^{-2}), slightly lower performance was observed, likely due to subtle variations in deposition conditions during scale-up. Furthermore, the same deposition strategy was applied to fabricate a 50 cm^2 electrode, which also demonstrated excellent uniformity. The HER performance measured at nine different points yielded an average overpotential of 18.3 mV at −10 mA cm^{-2}, with a remarkably low standard deviation of 0.81 mV.

Overall, this study highlights that precise control of deposition potential and interelectrode distance is critical when scaling up the electrochemical fabrication of alloy electrodes. It also provides a practical and reproducible fabrication methodology for extending high-performance lab-scale catalysts to industrial-scale applications.

ijer, 2026, 1, Downloaded from https://onlinelibrary.wiley.com/doi/10.1155/er/5468552 by MS HYEON - Chung-Ang University , Wiley Online Library on [24/03/2026]. See the Terms and Conditions (https://onlinelibrary.wiley.com/terms-and-conditions) on Wiley Online Library for rules of use; OA articles are governed by the applicable Creative Commons License

Author Contributions

Joon-Young Park: conceptualization, formal analysis, investigation, methodology, writing – original draft. **Kyeong-Rim Yeo:** conceptualization, formal analysis, writing – original draft. **Soo-Kil Kim:** conceptualization, funding acquisition, methodology, project administration, supervision, writing – review and editing.

Acknowledgments

This work was supported by the National Research Foundation of Korea (NRF) grant funded by the Korean Government (MSIT) (Grants RS-2024-00340074 and RS-2024-00413272). The authors used ChatGPT for English polishing during the manuscript preparation and acknowledge Editage for the final English editing.

Funding

This work was supported by the National Research Foundation of Korea (NRF) (Grants RS-2024-00340074 and RS-2024-00413272).

Conflicts of Interest

The authors declare no conflicts of interest.

Data Availability Statement

The data that support the findings of this study are available from the corresponding author upon reasonable request.

References

1. M. S. Dresselhaus and I. Thomas, "Alternative Energy Technologies," *Nature* 414 (2001): 332–337.

2. S. Chu and A. Majumdar, "Opportunities and Challenges for a Sustainable Energy Future," *Nature* 488, no. 7411 (2012): 294–303.

3. T. Ahmad and D. Zhang, "A Critical Review of Comparative Global Historical Energy Consumption and Future Demand: The Story Told so Far," *Energy Reports* 6 (2020): 1973–1991.

4. V. Ramanathan and Y. Feng, "Air Pollution, Greenhouse Gases and Climate Change: Global and Regional Perspectives," *Atmospheric Environment* 43, no. 1 (2009): 37–50.

5. B. Parida, S. Iniyan, and R. Goic, "A Review of Solar Photovoltaic Technologies," *Renewable and Sustainable Energy Reviews* 15, no. 3 (2011): 1625–1636.

6. S. Roga, S. Bardhan, Y. Kumar, and S. K. Dubey, "Recent Technology and Challenges of Wind Energy Generation: A Review," *Sustainable Energy Technologies and Assessments* 52 (2022): 102239.

7. M. Shoaib, I. Siddiqui, S. Rehman, S. Khan, and L. M. Alhems, "Assessment of Wind Energy Potential Using Wind Energy Conversion System," *Journal of Cleaner Production* 216 (2019): 346–360.

8. J. A. Turner, "Sustainable Hydrogen Production," *Science* 305, no. 5686 (2004): 972–974.

9. P. K. Nayak, S. Mahesh, H. J. Snaith, and D. Cahen, "Photovoltaic Solar Cell Technologies: Analysing the State of the Art," *Nature Reviews Materials* 4, no. 4 (2019): 269–285.

10. R. Wang, M. Mujahid, Y. Duan, Z.-K. Wang, J. Xue, and Y. Yang, "A Review of Perovskites Solar Cell Stability," *Advanced Functional Materials* 29, no. 47 (2019): 1808843.

11. M. Chatenet, B. G. Pollet, D. R. Dekel, et al., "Water Electrolysis: From Textbook Knowledge to the Latest Scientific Strategies and Industrial Developments," *Chemical Society Reviews* 51, no. 11 (2022): 4583–4762.

12. S. A. Grigoriev, V. N. Fateev, D. G. Bessarabov, and P. Millet, "Current Status, Research Trends, and Challenges in Water Electrolysis Science and Technology," *International Journal of Hydrogen Energy* 45, no. 49 (2020): 26036–26058.

13. K. Jiao, J. Xuan, Q. Du, et al., "Designing the Next Generation of Proton-Exchange Membrane Fuel Cells," *Nature* 595, no. 7867 (2021): 361–369.

14. N. A. A. Qasem and G. A. Q. Abdulrahman, "A Recent Comprehensive Review of Fuel Cells: History, Types, and Applications," *International Journal of Energy Research* 2024, no. 1 (2024): 7271748.

15. P. Simon and Y. Gogotsi, "Perspectives for Electrochemical Capacitors and Related Devices," *Nature Materials* 19, no. 11 (2020): 1151–1163.

16. Y. Wang, Y. Song, and Y. Xia, "Electrochemical Capacitors: Mechanism, Materials, Systems, Characterization and Applications," *Chemical Society Reviews* 45, no. 21 (2016): 5925–5950.

17. T. M. Gür, "Review of Electrical Energy Storage Technologies, Materials and Systems: Challenges and Prospects for Large-Scale Grid Storage," *Energy & Environmental Science* 11, no. 10 (2018): 2696–2767.

18. T. Terlouw, C. Bauer, R. McKenna, and M. Mazzotti, "Large-Scale Hydrogen Production via Water Electrolysis: A Techno-Economic and Environmental Assessment," *Energy & Environmental Science* 15, no. 9 (2022): 3583–3602.

19. T. Nguyen, Z. Abdin, T. Holm, and W. Mérida, "Grid-Connected Hydrogen Production via Large-Scale Water Electrolysis," *Energy Conversion and Management* 200 (2019): 112108.

20. C. U. Kim, E. D. Jung, Y. W. Noh, et al., "Strategy for Large-Scale Monolithic Perovskite/Silicon Tandem Solar Cell: A Review of Recent Progress," *EcoMat* 3, no. 2 (2021): 2021–e12084.

21. J. Li, Z. Li, Q. Sun, et al., "Recent Advances in the Large-Scale Production of Photo/Electrocatalysts for Energy Conversion and Beyond," *Advanced Energy Materials* 14, no. 45 (2024): 2402441.

22. Z. Li, T. R. Klein, D. H. Kim, et al., "Scalable Fabrication of Perovskite Solar Cells," *Nature Reviews Materials* 3, no. 4 (2018): 1–20.

23. X. Niu, N. Li, Q. Chen, and H. Zhou, "Insights Into Large-Scale Fabrication Methods in Perovskite Photovoltaics," *Advanced Energy and Sustainability Research* 2, no. 2 (2021): 2000046.

24. H. Sun, X. Xu, Z. Yan, et al., "Superhydrophilic Amorphous Co–B–P Nanosheet Electrocatalysts With Pt-Like Activity and Durability for the Hydrogen Evolution Reaction," *Journal of Materials Chemistry A* 6, no. 44 (2018): 22062–22069.

25. J. Kim, H. Kim, G. H. Han, et al., "Electrodeposition: An Efficient Method to Fabricate Self-Supported Electrodes for Electrochemical Energy Conversion Systems," in *Exploration*, (Wiley Online Library, 2022): 20210077.

26. P. Wang and B. Wang, "Interface Engineering of Binder-Free Earth-Abundant Electrocatalysts for Efficient Advanced Energy Conversion," *ChemSusChem* 13, no. 18 (2020): 4795–4811.

27. X.-L. Teng, X.-T. Sun, L. Guan, H. Hu, and M.-B. Wu, "Self-Supported Transition Metal Oxide Electrodes for Electrochemical Energy Storage," *Tungsten* 2, no. 4 (2020): 337–361.

28. Z. Zhao, H. Wu, H. He, X. Xu, and Y. Jin, "A High-Performance Binary Ni–Co Hydroxide-Based Water Oxidation Electrode With Three-Dimensional Coaxial Nanotube Array Structure," *Advanced Functional Materials* 24, no. 29 (2014): 4698–4705.

29. H. Liu, X. Cheng, Y. Chong, H. Yuan, J.-Q. Huang, and Q. Zhang, "Advanced Electrode Processing of Lithium Ion Batteries: A Review of Powder Technology in Battery Fabrication," *Particuology* 57 (2021): 56–71.

ijer, 2026, 1, Downloaded from https://onlinelibrary.wiley.com/doi/10.1155/er/5468552 by MS HYEON - Chung-Ang University , Wiley Online Library on [24/03/2026]. See the Terms and Conditions (https://onlinelibrary.wiley.com/terms-and-conditions) on Wiley Online Library for rules of use; OA articles are governed by the applicable Creative Commons License

30. H. Sun, Z. Yan, F. Liu, W. Xu, F. Cheng, and J. Chen, "Self-Supported Transition-Metal-Based Electrocatalysts for Hydrogen and Oxygen Evolution," *Advanced Materials* 32, no. 3 (2020): 1806326.

31. X.-Y. Zhang, W.-L. Yu, J. Zhao, B. Dong, C.-G. Liu, and Y.-M. Chai, "Recent Development on Self-Supported Transition Metal-Based Catalysts for Water Electrolysis at Large Current Density," *Applied Materials Today* 22 (2021): 100913.

32. Y. Li, J. Zhu, H. Cheng, et al., "Developments of Advanced Electrospinning Techniques: A Critical Review," *Advanced Materials Technologies* 6, no. 11 (2021): 2100410.

33. J. Xue, T. Wu, Y. Dai, and Y. Xia, "Electrospinning and Electrospun Nanofibers: Methods, Materials, and Applications," *Chemical Reviews* 119, no. 8 (2019): 5298–5415.

34. B. Joshi, E. Samuel, Y.-I. Kim, A. L. Yarin, M. T. Swihart, and S. S. Yoon, "Review of Recent Progress in Electrospinning-Derived Freestanding and Binder-Free Electrodes for Supercapacitors," *Coordination Chemistry Reviews* 460 (2022): 214466.

35. X. Xiong, W. Luo, X. Hu, et al., "Flexible Membranes of MoS2/C Nanofibers by Electrospinning as Binder-Free Anodes for High-Performance Sodium-Ion Batteries," *Scientific Reports* 5, no. 1 (2015): 9254.

36. Z. Cai, B. Liu, X. Zou, and H.-M. Cheng, "Chemical Vapor Deposition Growth and Applications of Two-Dimensional Materials and Their Heterostructures," *Chemical Reviews* 118, no. 13 (2018): 6091–6133.

37. L. Sun, G. Yuan, L. Gao, et al., "Chemical Vapour Deposition," *Nature Reviews Methods Primers* 1, no. 1 (2021): 5.

38. M. B. Kale, R. A. Borse, A. G. A. Mohamed, and Y. Wang, "Electrocatalysts by Electrodeposition: Recent Advances, Synthesis Methods, and Applications in Energy Conversion," *Advanced Functional Materials* 31, no. 25 (2021): 2101313.

39. S. A. Lee, J. W. Yang, S. Choi, and H. W. Jang, "Nanoscale Electrodeposition: Dimension Control and 3D Conformality," in *Exploration*, (Wiley Online Library, 2021): 20210012.

40. K. Choy, "Chemical Vapour Deposition of Coatings," *Progress in Materials Science* 48, no. 2 (2003): 57–170.

41. K.-R. Yeo, J. Eo, M. J. Kim, and S.-K. Kim, "Shape Control of Metal Nanostructures by Electrodeposition and Their Applications in Electrocatalysis," *Journal of The Electrochemical Society* 169, no. 11 (2022): 112502.

42. G. Yang, D. Deng, Y. Zhang, Q. Zhu, and J. Cai, "Numerical Optimization of Electrodeposition Thickness Uniformity With Respect to the Layout of Anode and Cathode," *Electrocatalysis* 12, no. 5 (2021): 478–488.

43. M.-H. Yeh, S.-J. Ho, G.-H. Chen, C.-W. Yeh, P.-R. Chen, and H.-S. Chen, "Toward Low-Cost Large-Area CIGS Thin Film III: Effect of Se Concentration on Crystal Growth and Defect Formation of Sequentially Electrodeposited CIGS Thin Films," *Solar Energy* 132 (2016): 547–557.

44. K.-R. Yeo, K.-S. Lee, H. Kim, J. Lee, and S.-K. Kim, "A Highly Active and Stable 3D Dandelion Spore-Structured Self-Supporting Ir-Based Electrocatalyst for Proton Exchange Membrane Water Electrolysis Fabricated Using Structural Reconstruction," *Energy & Environmental Science* 15, no. 8 (2022): 3449–3461.

45. K.-R. Yeo, H. Kim, K.-S. Lee, et al., "Controlled Doping of Ultralow Amounts Ru on Ni Cathode for PEMWE: Experimental and Theoretical Elucidation of Enhanced Performance," *Applied Catalysis B: Environment and Energy* 346 (2024): 123738.

46. C. H. Lee, K.-R. Yeo, and S.-K. Kim, "Highly Active and Durable NiMoMn Hydrogen Evolution Catalysts for Proton-Exchange Membrane Water Electrolysis," *International Journal of Energy Research* 2025, no. 1 (2025): 5812374.

47. K.-R. Yeo, H. S. Park, S. Ahn, S. H. Ahn, and S.-K. Kim, "Nanowire-Template-Assisted NiMo Catalyst for Efficient Hydrogen Evolution in Anion-Exchange Membrane Water Electrolyzers," *Applied Surface Science* 694 (2025): 162842.

48. L. Guo, J. Xie, S. Chen, et al., "Self-Supported Crystalline-Amorphous Composites of Metal Phosphate and NiS for High-Performance Water Electrolysis Under Industrial Conditions," *Applied Catalysis B: Environmental* 340 (2024): 123252.

49. K. J. Choi, H. Kim, and S.-K. Kim, "Multicomponent Nonprecious Hydrogen Evolution Catalysts for High Performance and Durable Proton Exchange Membrane Water Electrolyzer," *Journal of Power Sources* 506 (2021): 230200.

50. H. T. Bang, K.-R. Yeo, K. J. Choi, W. S. Jung, and S.-K. Kim, "Ternary Ni-Mo-P Catalysts for Enhanced Activity and Durability in Proton Exchange Membrane Water Electrolysis," *International Journal of Energy Research* 46, no. 9 (2022): 13023–13034.

51. T. Kim, K.-R. Yeo, H. Kim, J. Lee, and S.-K. Kim, "Impact of Phosphide–Phosphate Ratio on NiCoP Catalysts for Hydrogen Evolution in Anion Exchange Membrane Water Electrolysis," *International Journal of Energy Research* 2025, no. 1 (2025): 6685212.

52. K.-R. Yeo, H. Kim, L. Xu, et al., "Promoting Oxygen Evolution in Proton Exchange Membrane Water Electrolysis: Controlling the Oxidation State of Electrochemically Fabricated Iridium–cobalt Oxide Catalysts," *Journal of Energy Chemistry* 107 (2025): 881–893.

53. A. M. Ahmed, A. M. Abdelrahim, M. G. Abd El-Moghny, W. M. Morsi, and M. S. El-Deab, "Exceptional Electrocatalytic Performance of NiMoO4@ In-Situ Functionalized Graphite Felt Towards Hydrogen Evolution Reaction Utilizing a Facile Electrodeposition Process," *International Journal of Hydrogen Energy* 98 (2025): 708–718.

54. H. Zhang, F. Li, S. Ji, et al., "One-Step Electrodeposition of Cauliflower-Like Ni–Fe–Sn Particles as a Highly-Efficient Electrocatalyst for the Hydrogen Evolution Reaction," *International Journal of Hydrogen Energy* 45, no. 46 (2020): 24615–24625.

55. Z. Xing, D. Wang, T. Meng, and X. Yang, "Superb Hydrogen Evolution by a Pt Nanoparticle-Decorated Ni_3S_2 Microrod Array," *ACS Applied Materials & Interfaces* 12, no. 35 (2020): 39163–39169.

56. S.-Q. Chang, C.-C. Cheng, P.-Y. Cheng, C.-L. Huang, and S.-Y. Lu, "Pulse Electrodeposited FeCoNiMnW High Entropy Alloys as Efficient and Stable Bifunctional Electrocatalysts for Acidic Water Splitting," *Chemical Engineering Journal* 446 (2022): 137452.

57. J. Park, H. Kim, G. H. Han, et al., "Electrochemically Fabricated MoO_3–MoO_2@ NiMo Heterostructure Catalyst With Pt-Like Activity for the pH-Universal Hydrogen Evolution Reaction," *Journal of Materials Chemistry A* 9, no. 6 (2021): 3677–3684.

58. A. Kampmann, V. Sittinger, J. Rechid, and R. Reineke-Koch, "Large Area Electrodeposition of Cu (in, Ga) Se2," *Thin Solid Films* 361 (2000): 309–313.

59. S. Oh, H. Park, H. Kim, et al., "Fabrication of Large Area Ag Gas Diffusion Electrode via Electrodeposition for Electrochemical CO2 Reduction," *Coatings* 10, no. 4 (2020): 341.

60. B.-S. Lee, S. H. Ahn, H.-Y. Park, et al., "Development of Electrodeposited IrO2 Electrodes as Anodes in Polymer Electrolyte Membrane Water Electrolysis," *Applied Catalysis B: Environmental* 179 (2015): 285–291.

61. A. Karpuz, H. Kockar, and M. Alper, "The Effect of Different Chemical Compositions Caused by the Variation of Deposition Potential on Properties of Ni–Co Films," *Applied Surface Science* 257, no. 8 (2011): 3632–3635.

62. E. Pellicer, A. Varea, S. Pané, et al., "Nanocrystalline Electroplated Cu–Ni: Metallic Thin Films With Enhanced Mechanical Properties and Tunable Magnetic Behavior," *Advanced Functional Materials* 20, no. 6 (2010): 983–991.

ijer, 2026, 1, Downloaded from https://onlinelibrary.wiley.com/doi/10.1155/er/5468552 by MS HYEON - Chung-Ang University , Wiley Online Library on [24/03/2026]. See the Terms and Conditions (https://onlinelibrary.wiley.com/terms-and-conditions) on Wiley Online Library for rules of use; OA articles are governed by the applicable Creative Commons License

63. D. Goranova, G. Avdeev, and R. Rashkov, "Electrodeposition and Characterization of Ni–Cu Alloys," *Surface and Coatings Technology* 240 (2014): 204–210.

64. E. Beltowska-Lehman, E. Chassaing, and K. Vu Quang, "Electrodeposition of Ni-Cu-Mo Ternary Alloys From Citrate Electrolytes," *Journal of Applied Electrochemistry* 21, no. 7 (1991): 606–611.

65. S. N. A. Malek and Y. Mohd, "Effect of Deposition Potential on the Structure, Electrocatalytic Activity and Stability of Pt Films for Methanol Oxidation," *International Journal of Electrochemical Science* 12, no. 2 (2017): 1561–1571.

66. S. H. Ahn, H.-Y. Park, I. Choi, et al., "Electrochemically Fabricated NiCu Alloy Catalysts for Hydrogen Production in Alkaline Water Electrolysis," *International Journal of Hydrogen Energy* 38, no. 31 (2013): 13493–13501.

67. M. Cherkaoui, E. Chassaing, and K. Vu Quang, "Plating of Ni-Mo Alloy Coatings," *Advanced Materials and Manufacturing Processes* 3, no. 3 (1988): 407–418.

68. Y. Zeng, Z. Li, M. Ma, and S. Zhou, "In Situ Surface Raman Study of the Induced Codeposition Mechanism of Ni–Mo Alloys," *Electrochemistry Communications* 2, no. 1 (2000): 36–38.

69. E. Chassaing, K. Vu Quang, and R. Wiart, "Mechanism of Nickel-Molybdenum Alloy Electrodeposition in Citrate Electrolytes," *Journal of Applied Electrochemistry* 19, no. 6 (1989): 839–844.

70. E. Beltowska-Lehman and P. Indyka, "Kinetics of Ni–Mo Electrodeposition From Ni-Rich Citrate Baths," *Thin Solid Films* 520, no. 6 (2012): 2046–2051.

71. U. Sarac, R. M. Öksüzoğlu, and M. C. Baykul, "Deposition Potential Dependence of Composition, Microstructure, and Surface Morphology of Electrodeposited Ni–Cu Alloy Films," *Journal of Materials Science: Materials in Electronics* 23 (2012): 2110–2116.

72. L. Péter, "A Simple Electrodeposition Problem and the Abundant Knowledge It Subserves to Teach," *Journal of Solid State Electrochemistry* 28, no. 3-4 (2024): 1291–1303.

73. H. J. Biswal, P. R. Vundavilli, and A. Gupta, "Investigations on the Effect of Electrode Gap Variation Over Pulse-Electrodeposition Profile," in *IOP Conference Series: Materials Science and Engineering*, (IOP Publishing, 2019): 012046.

74. B. Lara-Lara and A. Fernández, "Influence of Electrode Position in the Electrolytic Cell Configuration for the Electrodeposition of Cu (In, Ga) Se2 Thin Films," *Journal of Materials Science: Materials in Electronics* 26 (2015): 5593–5602.

75. J. Ge and Y. Yan, "Controllable Multinary Alloy Electrodeposition for Thin-Film Solar Cell Fabrication: A Case Study of Kesterite Cu2ZnSnS4," *iScience* 1 (2018): 55–71.

76. S. Wang, X. Guo, H. Yang, et al., "Electrodeposition Mechanism and Characterization of Ni–Cu Alloy Coatings From a Eutectic-Based Ionic Liquid," *Applied Surface Science* 288 (2014): 530–536.

77. F. Zhang, J. Liu, I. Ivanov, et al., "Reference and Counter Electrode Positions Affect Electrochemical Characterization of Bioanodes in Different Bioelectrochemical Systems," *Biotechnology and Bioengineering* 111, no. 10 (2014): 1931–1939.

78. D. Rutz, F. Brauchle, P. Stehle, I. Bauer, and T. Jacob, "An Experimental Method to Determine the Measurement Error of Reference Electrodes Within Lithium-Ion Batteries," *ChemElectroChem* 10, no. 17 (2023): e202300216.

Supporting Information

Additional supporting information can be found online in the Supporting Information section. (*Supporting Information*)

Scheme S1: Schematics of the reference electrode fixture used for fabricating a scaled-up (10.2 cm^2) electrocatalyst: (a) top view and (b) (cross-sectional) side view. Scheme S2: Measurement positions for the (a) 10.2 and (b) 50 cm^2 electrocatalysts. Photographs of the (c) 10.2 and (d) 50 cm^2 electrocatalysts electrodeposited onto carbon paper. Figure S1: (a) Deposition current–time (*i–t*) and HER polarization curves measured at four positions of the scaled-up catalyst under different deposition potentials: (b) −1.5, (c) −1.8, (d) −1.9, (e) −1.95, (f) −2, (g) −2.3, and (h) −2.5 V_{SCE}. Figure S2: XRD patterns of bare carbon paper and scaled-up catalysts electrodeposited at various potentials (−1.5, −1.8, −1.9, −1.95, −2.0, −2.3, and −2.5 V_{SCE}), measured at position 1. Figure S3: (a) Deposition *i–t* curves and (b) comparison of integrated charges (C cm^{-2}) obtained from *i–t* curves measured at various d_{WE-CE}. Figure S4: FE-SEM images of the scaled-up electrocatalysts at four positions under different d_{WE-CE}: (a) 6, (b) 7, (c) 8, and (d) 9 cm. Figure S5: HER polarization curves measured at four positions of the scaled-up catalyst under different d_{WE-CE}: (a) 6, (b) 6.5, (c) 7, (d) 7.5, (e) 8, (f) 8.5, and (g) 9 cm. Figure S6: (a) Deposition *i–t* and HER polarization curves measured at four positions of the scaled-up catalyst under different d_{WE-RE}: (b) 1.95, (c) 3.15, and (d) 3.65 cm. Figure S7: FE-SEM images of the scaled-up electrocatalysts at four positions under different d_{WE-RE} (a) 1.95, (b) 3.15, and (c) 3.65 cm. Figure S8: HER polarization curves measured at nine positions of the scaled-up 50 cm^2 catalyst.

ijer, 2026, 1, Downloaded from https://onlinelibrary.wiley.com/doi/10.1155/er/5468552 by MS HYEON - Chung-Ang University , Wiley Online Library on [24/03/2026]. See the Terms and Conditions (https://onlinelibrary.wiley.com/terms-and-conditions) on Wiley Online Library for rules of use; OA articles are governed by the applicable Creative Commons License